Hindawi
Journal of Sensors
Volume 2024, Article ID 6938870, 13 pages
https://doi.org/10.1155/2024/6938870

Research Article

Research on the Factors Influencing the Seismic Performance of Grouting Sleeve Assembled Double-Column Piers

Sheng Li,[1] **Zewen Yao**,[1] **Li Wang**,[1] **Li Ma**,[1] **Yongze He**,[1] **and Xuefeng Ban**[2]

[1]*College of Civil Engineering, Lanzhou Jiaotong University, Lanzhou, Gansu 730070, China*
[2]*China Railway Investment and Construction Group Co., Ltd., Beijing 102600, China*

Correspondence should be addressed to Sheng Li; ligwin@126.com

Received 14 November 2023; Revised 5 January 2024; Accepted 22 February 2024; Published 11 March 2024

Academic Editor: Sheng Du

The present study investigated the influence of key design parameters on the seismic performance of prefabricated precast assembled piers' connection parts to better adapt to the industrialized construction of prefabricated precast assembled pier connected using grouting sleeves. Relying on a prefabricated assembled bridge in the actual project, the ABAQUS software was used to establish a refined solid finite element model of prefabricated assembled piers connected with grouting sleeves. Numerical simulation analysis was conducted for the piers with low circumferential reciprocating loading. The seismic performance of the prefabricated assembled piers was evaluated in terms of hysteresis characteristics, dissipation characteristics, and damage development. The effects of the length of the grouting sleeve and the diameter of the longitudinal reinforcement on the seismic performance were also investigated. The maximum error between the numerical simulation results and the test results was 5.7%, and the plastic region of the precast assembled pier obtained from the numerical simulation was consistent with the test results, indicating that the numerical simulation method is accurate and reliable. When the length of the grouting sleeve increased from 0.6 to 1.2 m, the yield load, peak load, and dissipation of energy of prefabricated assembled piers increased by 11.6%, 10.9%, and 11.4%, respectively; no significant change in residual displacement; ductility coefficient decreased by a small amount. When the longitudinal reinforcement diameter increased from 20 to 50 mm, prefabricated assembled piers yield load, peak load, and dissipation increased by 99.6%, 89.3%, and 218.9%, respectively, whereas the residual displacement increased by 137.3%, and the ductility coefficient decreased more. Increasing the length of the grouting sleeve or increasing the diameter of longitudinal reinforcement improved the stiffness of the piers, causing the piers to displace less and damage less under the same force, but the residual displacement would increase.

1. Introduction

With the implementation and execution of the green highway construction concept, it is necessary to develop a prefabricated assembled bridge structural system to adapt to the industrialized construction technology of "factory prefabrication + on-site installation" to improve the production efficiency and guarantee the quality of the construction, and reduce the environmental effect of highway construction. The prefabricated assembled bridge has the advantages of a short construction period, green environmental protection, high safety, strong applicability to complex environments, and minimal effect on the surrounding environment, and its expanding application scope is one of the important trends in the development of the construction industry [1–7]. However, the application of prefabricated assembled bridges in earthquake-prone areas is minimal, and many countries only use prefabricated assembled bridges in low-intensity areas because the seismic theory of assembled bridges is not yet perfect.

The connection forms of precast assembled bridges include primarily grouting sleeve connection, grouting bellows connection, socket connection, and prestressing tendon connection, with the grouting sleeve connection being one of the most widely used connection methods. Different connection methods between the components of precast assembled bridges lead to modifications to the mechanical model of the bridges; there are significant differences in their response and damage modes under the effect of earthquakes. For

conventional monolithic concrete bridges, when an earthquake occurs, concrete cracking, spalling, and reinforcement yielding appear at the top or bottom of the pier, and the connection parts of each component are prone to tensile cracks. By contrast, in precast assembled bridge piers during earthquakes, openings are formed in the joints between the various components, the concrete crushes at the contact parts of the components when the compressive stress at the joints is too large, and the damage is concentrated primarily on the pier parts. Therefore, our study focused on the seismic performance of the pier part on prefabricated assembled bridges [8, 9].

Scholars have focused on prefabricated assembled bridges through proposed static tests, shaking table tests, numerical simulation analysis, and theoretical analysis to clarify the seismic performance and damage mode of prefabricated assembled bridges. The first damaged part during earthquakes is the part of the bridge pier connecting with the pier and the cover girder, and the damage mode is the ductile damage dominated by the bending damage. The seismic performance of prefabricated assembled piers is affected by the reinforcement rate, concrete strength, axial pressure ratio, pier aspect ratio, and other factors [10–23]. When a prefabricated assembled bridge uses a socket connection, the embedded depth of the socket structure is different, and the prefabricated precast assembled pier damage mode is not the same. When the depth of burial is equal to double the diameter of the columns, socket pier bearing capacity and cast-in-place piers are the same, but the energy-consuming capacity and displacement ductility are not as good as the cast-in-place piers. When the burial depth is one and a half times the diameter of the columns, the socket pier bearing capacity, energy consumption capacity, and ductility are better than cast-in-place piers [24]. When prefabricated assembled piers use the grouting sleeve connection, their seismic performance is determined by the location of the grouting sleeve, grout strength, grouting sleeve length, and other factors. When the grouting sleeve is located at the top of the bearing platform, the response of the precast collocated bridge under seismic action is consistent with that of a conventional monolithic bridge. When the grouting sleeve is located at the bottom of the pier, the prefabricated assembled bridge has greater stiffness but worse ductility, and the energy dissipation capacity of both is close to that of the conventional monolithic pier [25, 26]. To improve the seismic performance of prefabricated assembled bridges and reduce the damage of prefabricated assembled bridges under seismic action, researchers have taken a series of measures: adding prestressing tendons in the pier, adding carbon fiber cloth outside the pier, and adding dampers and built-in rubber mats. Stacked rubber mats in precast assembled piers effectively reduce localized concrete damage and increase the energy-consuming capacity of the bridge pier [17, 27, 28].

Current research on precast assembled piers has focused primarily on optimizing connection mode, comparison of different connection modes, and damage modes. However, less research has been conducted on the effect of connection parameters of the grouting sleeve on its mechanical properties and seismic performance. The use of grouting sleeve connection piers and pier with too small steel bar diameter, insufficient anchorage length, or too short sleeve leads to low precast assembled pier bearing capacity and no solid connection, thereby producing a large gap or even separation in piers and pier, whereas the use of grouting sleeve connection piers and pier with too large steel bar diameter or too long sleeve results in high cost and material waste. Therefore, based on the proposed static force method to impose horizontal reciprocating displacement on the bridge pier, through the control variables to study the grouting sleeve length, rebar diameter on the grouting sleeve-connected precast assembled pier seismic performance and damage development of the effect of the precast assembled pier, for the precast assembled pier design to provide reference and theoretical basis.

2. Numerical Analysis

The present study considered an assembled bridge in the Jining Inner Ring Elevated and Connection Project as a prototype. The dimensions of the bridge are shown in Figure 1. The grouting sleeve was located at the bottom of the pier, with a length of 800 mm, an outer diameter of 95 mm, an inner diameter of 40 mm, a longitudinal reinforcement with a diameter of 40 mm, and reinforcement bars at the two ends extending into the sleeve by 400 mm. The arrangement of the reinforcement bars and grouting sleeves is presented in Figure 2.

2.1. Numerical Simulation Program. To study the seismic performance of assembled piers, we analyzed the effect of sleeve length and rebar diameter on the seismic performance and damage development. We established a bridge pier model based on the control variable method using finite element software ABAQUS to analyze the seismic performance of assembled piers. Numerical simulation program specimen parameters were set, as revealed in Table 1. The specimen piers, cover beams, and bearing platforms were the same size, assembled pier by the pier, cover beams, bearing platforms, grouting sleeve, reinforcing steel five parts of the specimen sleeve length and reinforcing steel diameter are listed in Table 1. Group B specimens (Specimens A, B1, B2, and B3) were used to study the effect of sleeve length on the seismic performance of the assembled pier, whereas Group C specimens (Specimens A, C1, C2, and C3) were used to study the effect of reinforcing bar diameter on the seismic performance of the assembled pier.

2.2. Unit Types and Material Architecture. During the modeling process, the piers, cover beams, bearing platforms, reinforcement, and sleeves were modeled using 3D solid units. The concrete components, such as piers, cover beams, and bearing platforms, and the steel components, such as reinforcement and sleeves, were simulated using the eight-node hexahedral linear shrinkage integral unit (C3D8R).

The concrete grade used for piers was C50, the concrete grade used for cover girders and bearing platforms was C35, the sleeve material was high-strength ductile iron, and the reinforcement grade was HRB400. The grouting sleeve adopted the ideal elasticity model, with a density of 7,800 kg/m^3, a modulus of

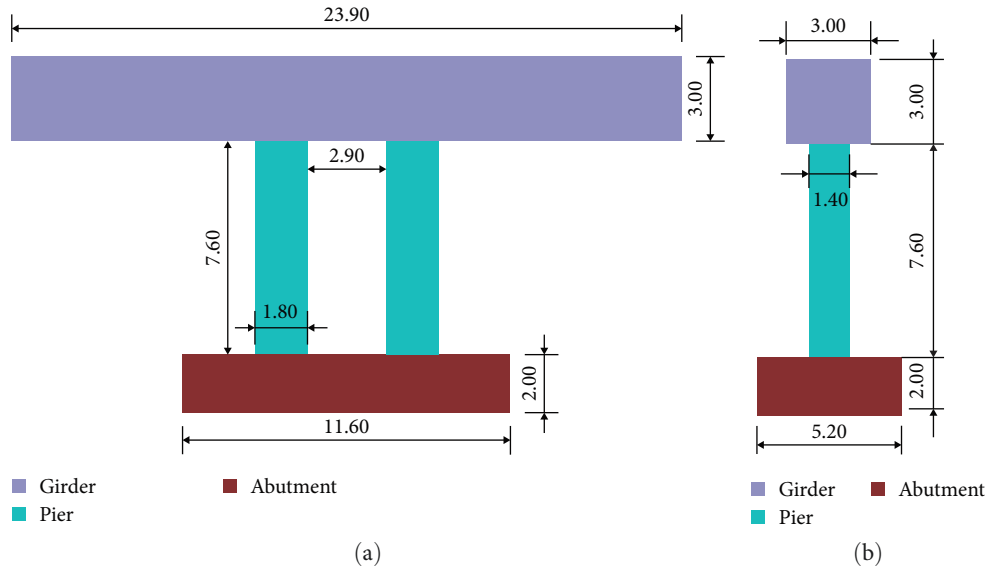

Figure 1: Dimensional detail of precast assembled pier (unit: m): (a) main view; (b) side view.

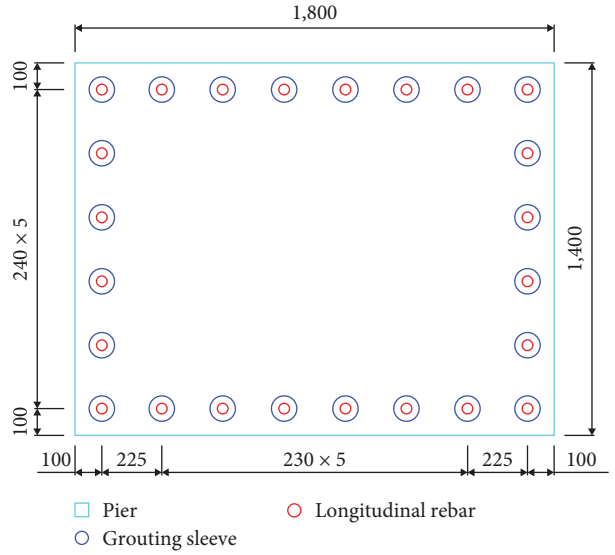

Figure 2: Detailed drawing of grouting sleeve arrangement form (unit: mm).

Table 1: Specimen parameters.

Specimen	A	B1	B2	B3	C1	C2	C3
Length of sleeve (h/m)	0.8	0.6	1.0	1.2	0.8	0.8	0.8
Diameter of reinforcement (D/mm)	40	40	40	40	20	30	50

elasticity of 2.1×105 MPa, and a Poisson's ratio of 0.3. The reinforcing steel adopted an ideal elastic–plastic model, with a density of 7,850 kg/m³, an elastic modulus of 2.1×105 MPa, a Poisson's ratio of 0.3, and a yield strength of 450 MPa. Concrete material selected the concrete damaged plasticity [29], with a density of 2,450 kg/m³, an elastic modulus of 3.25×104 MPa, and a Poisson's ratio of 0.2; the remaining parameters of the concrete material are shown in Table 2.

2.3. Contact Definition and Meshing. When performing ABAQUS simulation calculations, the selection of the contact relationship between the model components and the mesh division are crucial factors for the convergence and accuracy of the numerical simulation. Therefore, the appropriate contact relationship must be chosen based on the contact situation and contact material between the components. Under earthquake action, the bottom of the bridge pier and the

Table 2: Concrete material parameters.

Materials	Shear angle	k	fb0/fc0	Offset	Coefficient of viscosity
Concrete	30	0.6667	1.16	0.1	0.0001

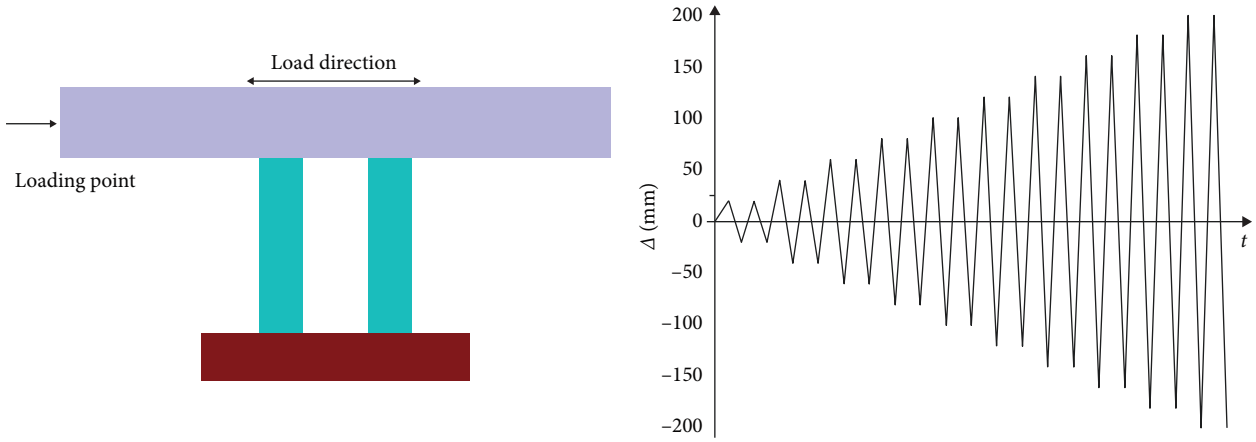

Figure 3: Schematic diagram of the loading system: (a) loading direction; (b) loading system.

bearing platform will slip between the selected surface-to-surface contact relationship. In the actual project, the rebar and the sleeve, through the combination of high-strength nonshrink cement grout, according to the actual situation of modeling, will lead to higher computational costs and convergence difficulty; therefore, in the modeling process, the rebar and sleeve through the high-strength nonshrink cement grout connection was simplified to a steel grout connection, and then the contact relationship was simplified to a steel grout connection. The cement grout connection was simplified to rebar and sleeve contact, considering a small slip between the rebar and sleeve under seismic action, and the surface-to-surface contact relationship was selected for simulation. The contact relationship was used to stimulate between the pier and the cover beam. There was no relative slip between the rebar, sleeve, pier, and bearing platform, so the embedded region contact relationship was used. The embedded region contact relationship was also used, as there was no relative slip between the reinforcement, pier, and bearing platform. In the modeling process, structured grid technology was used to divide each component into hexahedral cells, and the cell types of each component were C3D8R linear shrinkage integral cells [30].

2.4. Boundary Conditions and Loading Regime. Boundary conditions were applied to the model with full restraint at the bottom of the pier, i.e., limiting displacement and rotation in the x, y, and z directions. Considering the role of the bridge superstructure, after applying the self-weight effect to the pier model, a uniform load was applied at the top of the cover girder to simulate the weight of the superstructure. The proposed static method was used to simulate the seismic action by applying a low weekly reciprocating load to the precast assembled pier. The loading form was displacement control, and each cyclic process was divided into forward and reverse displacement loadings. The loading point was at the center of the left side face of the cover girder, and the loading direction was in the direction of the transverse bridge. The loading point and the loading direction are displayed in Figure 3.

3. Calibration of Numerical Analysis Results

To verify the reliability of the numerical simulation method, we referred to the established proposed static test of the assembled bridge connected using grouting sleeves. A finite element model of the precast assembled piers in the test was established based on the modeling method described in this section. After computing and analyzing the numerical simulation results, the numerical simulation results were compared with the test results.

3.1. Introduction to the Test Program. In order to validate the numerical simulation method used in this paper [31], the PCTS specimens from the literature were selected, the specimen PCTS was selected as the object of study, and the dimensions of the pier model are presented in Figure 4. The arrangement of grouting sleeves and longitudinal reinforcement of the pier cross-section is displayed in Figure 5. The parameters of the steel reinforcement grouting sleeves and the concrete aligned with the parameters of the test material; the contact relationship, the mesh delineation adopted the rules described in this chapter. The loading system aligned with the loading system of the test.

3.2. Numerical Simulation Verification. The finite element model of the precast assembled pier was established, operated, and analyzed based on the test parameters and the modeling method. Figure 6 shows the results of the numerical analysis

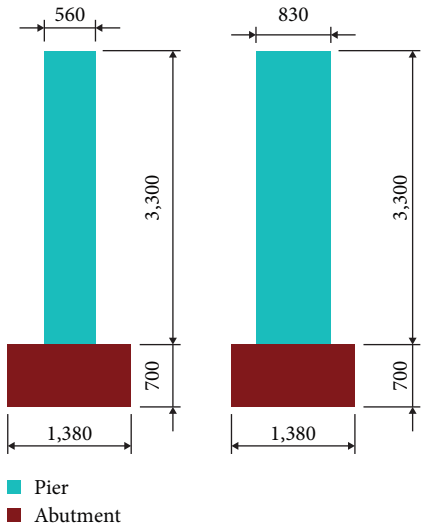

Figure 4: Details of specimen size (unit: mm).

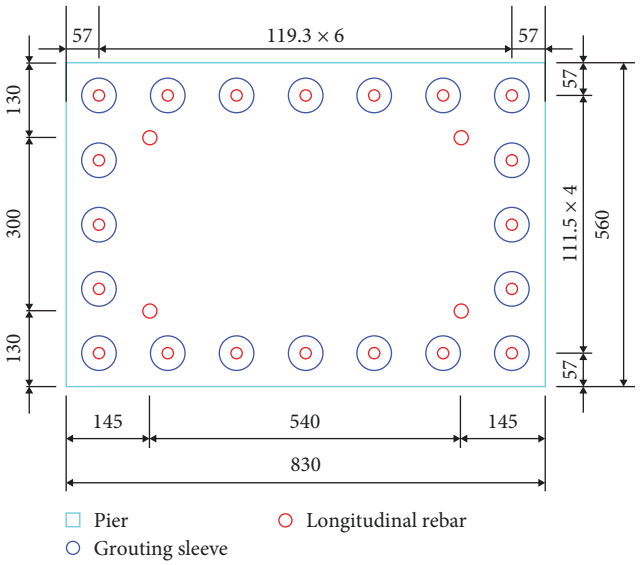

Figure 5: Column section reinforcement diagram (unit: mm).

of the bridge pier model obtained under the loading regime of the test and the comparative analysis of the skeleton curve of the results from established trials, indicating that the numerical simulation and the skeleton curve obtained from the test parameters have the same trend, and the values are very close.

A comparison of the strength and deformation characteristic values of the load–displacement curves of the assembled pier model during the loading process is presented in Table 3, demonstrating that the strength and deformation characteristic values of the numerical simulation and the test values were very close. The maximum error between the simulation results and the test results was 5.7%, indicating that the results obtained by the numerical simulation are accurate.

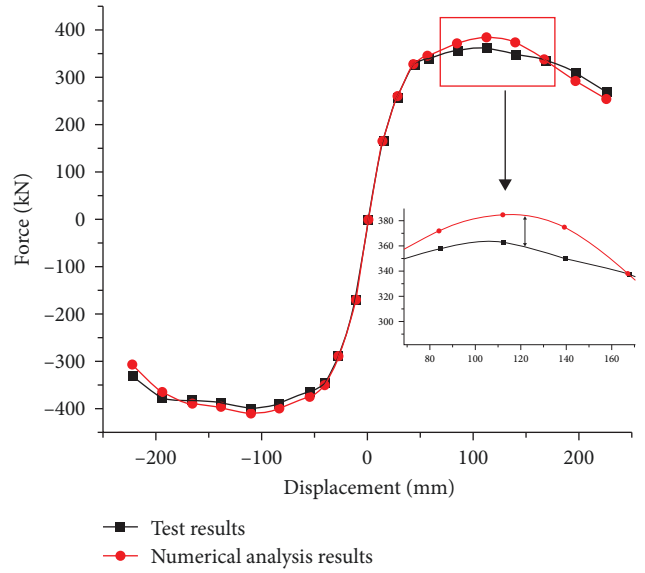

Figure 6: Comparison of experimental and numerical simulated skeleton curves.

4. Analysis of Influencing Factors

4.1. Sleeve Length

4.1.1. Hysteresis Performance

(1) Hysteresis Curve. The hysteresis curve of Group B specimens (Figure 7(a))—obtained after loading the finite element model of Group B specimens—revealed that the load-carrying capacity of Group B specimens decreased significantly after reaching the maximum value. The order from large to small load-carrying capacity was Specimens C3, C2, A, and C1 when the displacements were equal, and the load-carrying capacity of Specimen C3 was larger than that of the other three specimens with the increase in the displacements.

(2) Skeleton Curve. The shape of the Group B pier model skeleton curve (Figure 7(b)) was close to the first linear rise, followed by a slower rate of rise into the plastic phase, and then began to decline. Group B pier model strength and deformation characteristics of the numerical values are presented in Table 4, combined with the skeleton curve of Group B specimens. Group B pier model reached the peak load before, i.e., the OP section, the load-carrying capacity with the increase in displacement. In the Group B pier model, after reaching the peak displacement, i.e., the PQ section, the bearing capacity with the displacement increased and then decreased. Group B pier model in the displacement was equal to its bearing capacity. The order from large to small bearing capacity was Specimens B3, B2, A1, and B1. For Specimens B3, B2, A1, and B1, the yield loads were 12,840.7, 12,318.3, 12,148.7, and 11,500.6 kN, respectively; the peak loads were 15,300.0, 14,300.0, 1,400.0, 11,500.6 kN, respectively; the yield displacements were 33.06, 32.57, 32.10, and 31.41 mm, respectively. The peak displacements were close to each other, i.e., the greater the length of the grouting sleeve, the maximum load-carrying capacity of the

Table 3: Numerical values of strength and deformation characteristics obtained from tests and numerical simulations.

	Test results	Numerical simulation results	Inaccuracies (%)
Yield force (kN)	323.1	338.7	4.8
Yield displacement (mm)	40.6	38.5	5.2
Ultimate force (kN)	364.3	385.3	5.7
Limit displacement (mm)	207.2	195.9	5.4

precast assembled pier connected using grouting sleeves, and the length of the grouting sleeve increased from 0.6 to 0.8, 1.0, and 1.2 m; its yield load increased by 5.6%, 7.1%, and 11.6%, respectively; its peak load increased by 2.2%, 2.9%, and 10.9%, respectively; its yield displacement decreased by 1.5%, 2.9%, and 5.0%, respectively. The ultimate displacement was close, but the increase in the grouting sleeve length decreased the ductility coefficient of the precast assembled pier.

(*3) Cumulative Energy Dissipation*. From the cumulative hysteretic energy dissipation of the Group B pier model (Figure 7(c)), the cumulative hysteretic energy dissipation of the Group B pier model increased with the increase in loading displacement. During the loading process, the order from the weakest to the strongest energy dissipation capacity of the Group B pier model was B1, A1, B2, and B3, and the cumulative energy dissipation of B1, A1, B2, and B3 was 25,437.0, 26,513.6, 26,690.8, and 28,332.5 kN m, respectively. Therefore, the longer the length of the grouting sleeve, the stronger the energy dissipation capacity of grouting sleeve-connected assembled piers. The highest cumulative energy dissipation was 28,332.5 kN m. When the length of the grouting sleeve was increased from 0.6 to 0.8, 1.0, and 1.2 m, the cumulative dissipated energy of the grouting sleeve increased by 4.2%, 4.9%, and 11.4%, respectively. The longer the length of the grouting sleeve, the stronger the energy dissipation capacity of the precast assembled pier connected using grouting sleeves, and the safer the bridges will be under seismic action.

(4) Residual Displacement. From the residual displacements of Group B specimens (Figure 7(d)), the residual displacements of Group B pier models increased with the increase in loading displacement. The length of the grouting sleeve did not have a significant effect on the residual displacements of the precast assembled pier connected using the grouting sleeve.

4.1.2. Damage Mechanism. The damage mechanism of the bridge pier mainly included stress development and plastic region development. Group B pier model peak displacement was around 60 mm. Therefore, when analyzing the damage mechanism of the assembled bridge pier, the stress cloud and plastic region cloud were extracted when the forward displacement of the pier model reached 60 mm for the first time.

(1) Stress Development. From the stress cloud diagram of the Group B pier model (Figure 8), the Group B pier model in the displacement loading process at the top of the pier, the pier lower grouting sleeve upper region, and the bottom of the pier appeared stress concentration; grouting sleeve length changes, only the pier lower grouting sleeve upper region of the stress concentration area with the change, the remaining two stress concentration area unchanged.

(2) Plastic Region Development. From the plastic region cloud diagram of the Group B pier model (Figure 9), the plastic region of the upper and lower part of pier model B1 was the largest and the lowest position, and the plastic region of the middle part of the pier was the smallest, and the plastic region of the upper and lower part of pier model B3 was the smallest and the highest position, and the plastic region of the middle part of the pier was the largest. The plastic region of the lower part of the pier of the assembled bridge pier was above the grouting sleeve and increased with the increase in the length of the grouting sleeve, and the area of its plastic region decreased with the increase in the length of the grouting sleeve, but the area of the plastic region of the central part of the pier increased with the increase in the length of the grouting sleeve.

4.2. Reinforcement Diameters

4.2.1. Hysteresis Performance

(1) Hysteresis Curve. The operation analysis was based on the numerical simulation method to establish the finite element model. From the hysteresis curve of the Group C pier model (Figure 10(a)), the hysteresis curves of the Group C pier model were in the shape of steps.

(2) Skeleton Curve. From the skeleton curve of the Group C pier model (Figure 10(b)), the skeleton curve shape was close to the first linear rise, which then entered the plastic phase. The rise speed became slower, which then began to decline. In the loading process, the order of large to small pier model bearing capacity was C3, A1, C2, and C1. From Group C pier model strength and deformation characteristics (Table 5) combined with the skeleton curve of Group C specimens, the bearing capacity of Group C bridge pier model before reaching the peak load increased with the increase in displacement; after reaching the peak load, the bearing capacity decreased with the increase in displacement. The yield loads of bridge pier models C3, A1, C2, and C1 were 15,328.2, 12,148.7, 9,515.1, and 7,678.2 kN, respectively; the peak loads were 17,000.0, 14,100.0, 11,400.0, and 8,980.0 kN, respectively; the yield displacements were 21.66, 25.73, 32.57, and 35.47 mm, respectively. The larger the diameter of the longitudinal reinforcement bars, the greater the yield loads, peak loads, yield displacements, and peak displacements of the precast assembled pier connected using grouted sleeves. When the diameter of longitudinal reinforcement was increased from 20 to 30, 40, and 50 mm, the yield load increased by 23.9%, 58.2%, and 99.6%, respectively; the peak load increased by 26.9%, 57.0%, and 89.3%, respectively; the

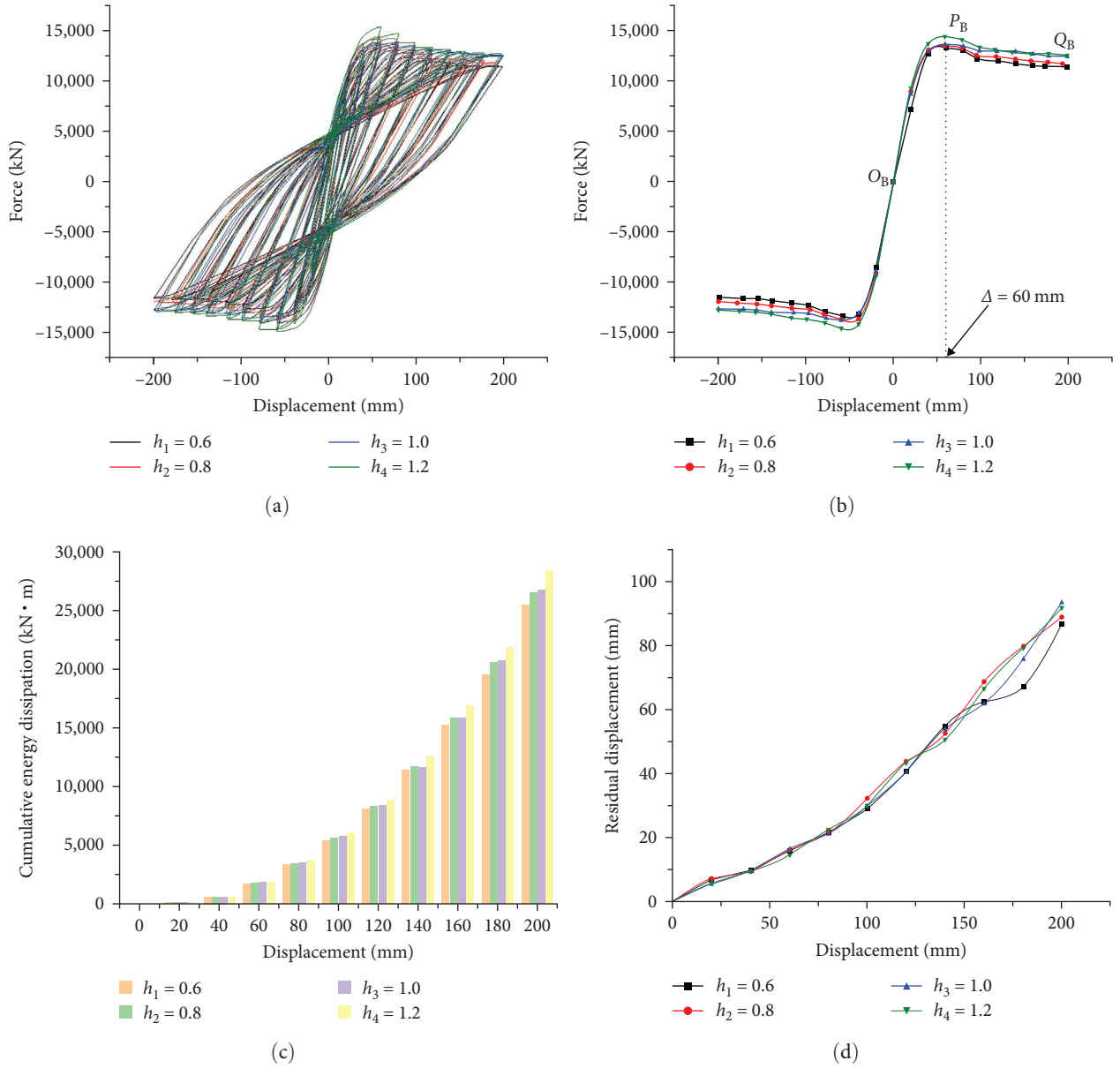

Figure 7: Hysteresis performance curves of Group B pier model: (a) hysteretic curve; (b) skeleton curve; (c) cumulative energy dissipation; (d) residual displacement.

Table 4: Group B pier model strength and deformation characteristics of numerical value.

Specimen	Load direction	Yield		Ultimate		Ductility factor
		Force (kN)	Displacement (mm)	Force (kN)	Displacement (mm)	
B1	Positive	11,696.8	33.06	13,800.0	59.95	5.93
	Negative	11,500.6	28.46	13,500.0	58.41	7.52
A	Positive	11,907.0	32.57	14,100.0	59.80	5.72
	Negative	12,148.7	30.15	13,900.0	58.66	7.04
B2	Positive	11,205.1	32.10	14,200.0	59.42	5.48
	Negative	12,318.3	31.96	14,000.0	59.70	7.02
B3	Positive	12,231.1	31.41	15,300.0	59.48	5.39
	Negative	12,840.7	31.14	14,900.0	59.45	6.98

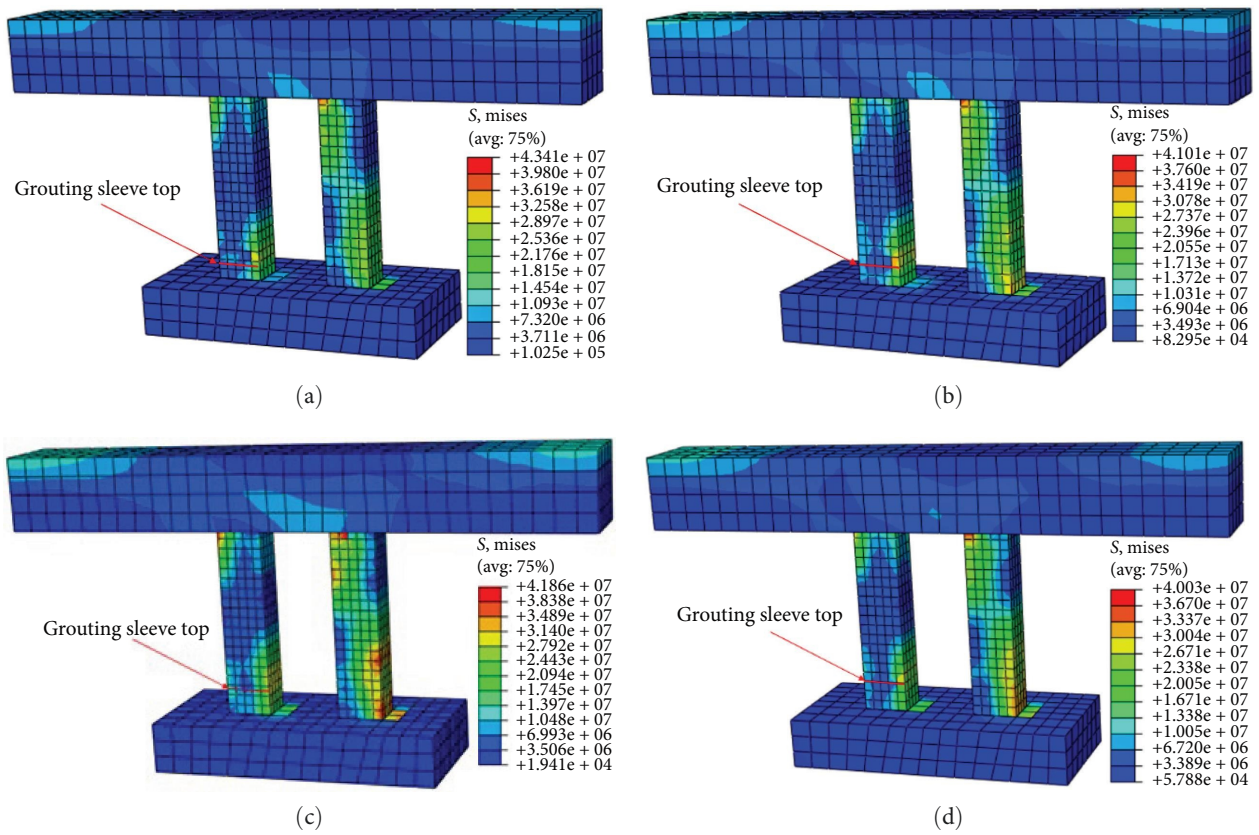

Figure 8: Stress cloud of Group B pier model displacement loaded to 60 mm: (a) Specimen B1; (b) Specimen A; (c) Specimen B2; (d) Specimen B3.

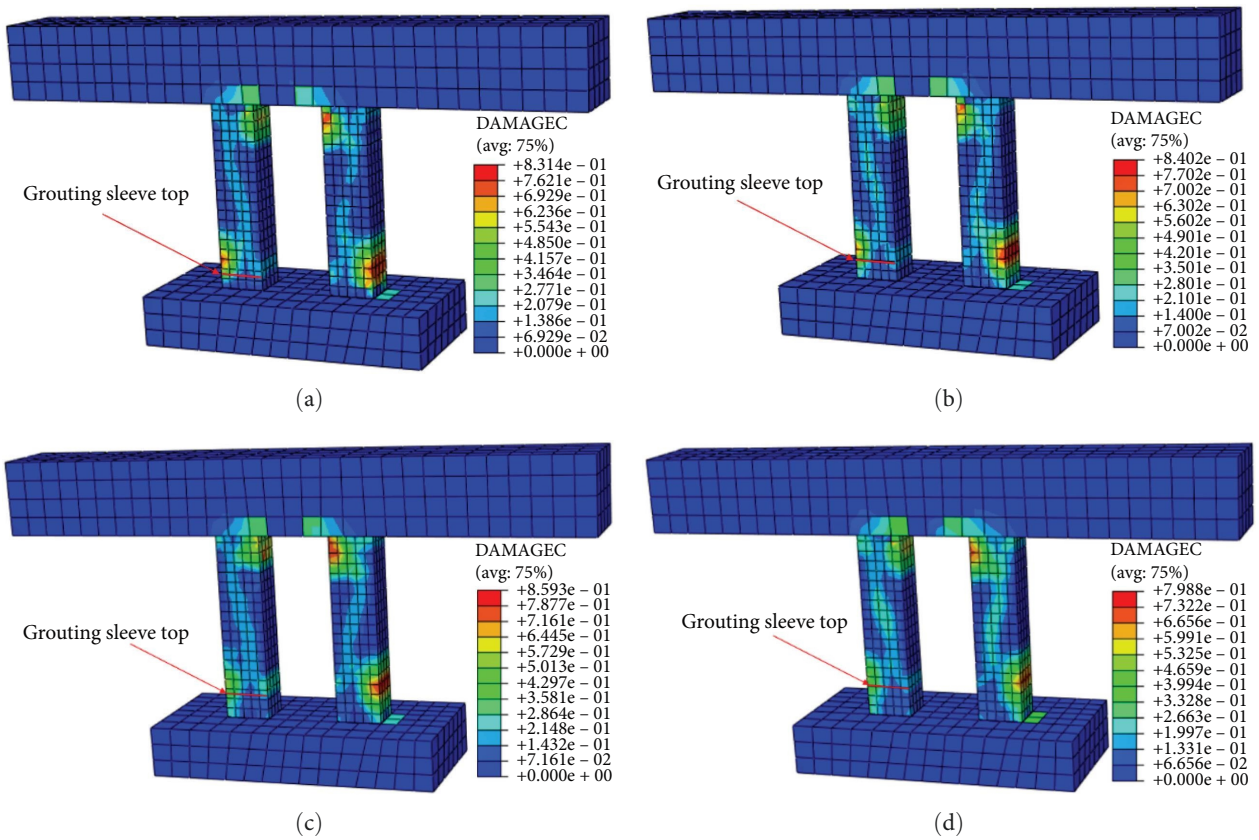

Figure 9: Plastic region cloud of Group B pier model displacement loaded to 60 mm: (a) Specimen B1; (b) Specimen A; (c) Specimen B2; (d) Specimen B3.

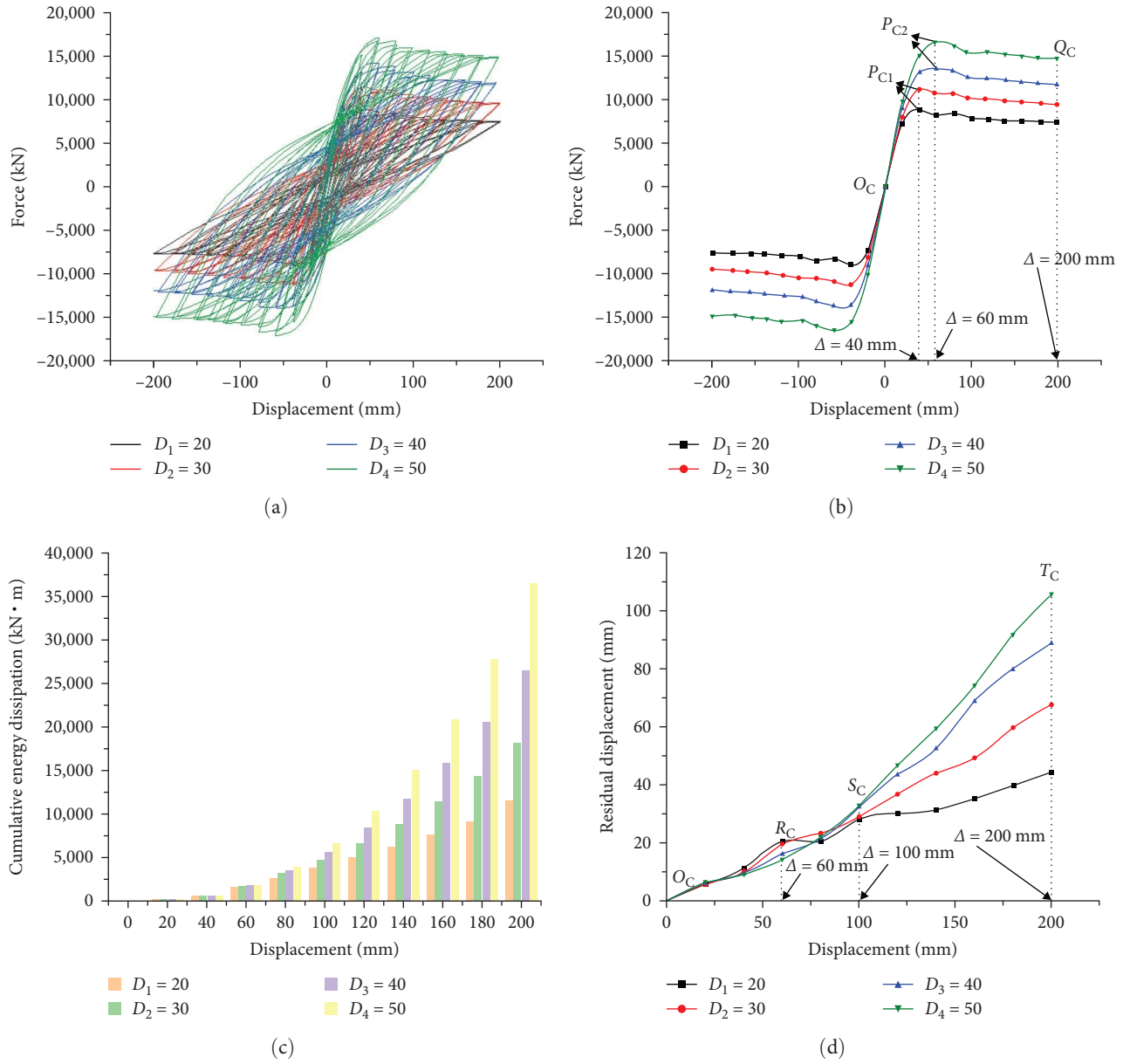

Figure 10: Hysteresis performance curves of Group C pier model: (a) hysteretic curve; (b) skeleton curve; (c) cumulative energy dissipation; (d) residual displacement.

Table 5: Group C pier model strength and deformation characteristics of numerical value.

Specimen	Load direction	Yield		Ultimate		Ductility factor
		Force (kN)	Displacement (mm)	Force (kN)	Displacement (mm)	
C1	Positive	7,515.5	21.66	8,800.0	44.90	9.18
	Negative	7,678.2	18.67	8,980.0	39.42	10.79
C2	Positive	9,097.2	25.73	11,400.0	43.99	7.03
	Negative	9,515.1	21.11	11,100.0	58.78	10.09
A	Positive	11,907.0	32.57	14,100.0	59.80	5.72
	Negative	12,148.7	30.15	13,900.0	58.66	7.04
C3	Positive	14,965.4	38.05	17,000.0	59.87	5.61
	Negative	15,328.2	35.47	17,000.0	59.82	6.70

yield displacement increased by 18.8%, 50.4%, and 63.7%, respectively. The peak displacement also increased, but the coefficient of ductility decreased.

(3) Accumulated Energy Dissipation. The cumulative hysteretic dissipation energy (Figure 10(c)) of Group C specimens revealed that the cumulative hysteretic dissipation energy of Group C pier models increased with the increase in loading displacement. During the loading process, the order of weak to strong energy dissipation capacity of Group C pier models was C1, C2, A1, and C3, and their cumulative energy dissipation values were 11,447.0, 18,215.8, 26,513.6, and 36,510.7 kN m, respectively; during the loading process, the larger the diameter of the reinforcement, the stronger the energy dissipation capacity of the precast assembled pier connected using the grouting sleeve, and the more the cumulative dissipated energy; the diameter of the longitudinal reinforcement increased from 20 to 30, 40, and 50 mm, and the cumulative dissipated energy increased by 59.1%, 131.6%, and 218.9%, respectively.

(4) Residual Displacement. The residual displacement of the Group C specimen (Figure 10(d)) revealed that the residual displacement of the Group C pier model increased with the increase in loading displacement; pier model displacement loaded between 0 and 60 mm (O_CR_C segment), the descending order of residual displacement of Group C pier model was C1, C2, A1, and C3, pier model displacement loaded between 100 and 200 mm (S_CT_C segment), the descending order of residual displacement of Group C pier model was C3, A1, C2, and C1, loaded to 200 mm (T_C point), pier model C1, C2, A1, and C3 residual displacements were 44.6, 67.7, 89.1, and 105.8 mm; combined with the skeleton curve of the bridge pier model of Group C, the relationship between its bearing capacity and residual displacement revealed that precast assembled piers in the overall elastic stage and part of the elastic–plastic stage, before reaching the ultimate bearing capacity. The smaller the diameter of longitudinal reinforcement, the greater the residual displacement. When the diameter of the reinforcement increased from 20 to 30, 40, and 50 mm, the residual displacement decreased by 5.3%, 20.9%, and 30.1%, respectively, after the precast assembled pier to the plastic stage, in the process of bearing capacity decrease. The larger the diameter of longitudinal reinforcement, the larger the residual displacement, and when the diameter of reinforcement increased from 20 to 30, 40, and 50 mm, its residual displacement increased by 51.8%, 99.8%, and 137.2%, respectively. The larger the diameter of the longitudinal reinforcement, the larger the residual displacement of the prefabricated assembled bridge abutment connected by the grouting sleeve after entering the plastic phase, and the more difficult it was to reset the bridge after the earthquake, so the diameter of the longitudinal reinforcement should not be too large when carrying out the design work of the bridge to prevent the bridge from being difficult to reset after the earthquake.

4.2.2. Damage Mechanism. The damage mechanism of the bridge pier includes stress development and plastic region development in two aspects. Group C pier model reached the peak load displacement of about 40 and 60 mm, so the analysis of the damage mechanism of the assembled bridge pier to extract the forward displacement of the pier model for the first time reached 60 mm with the extraction of the stress cloud map and plastic region cloud map.

(1) Stress Development. From the stress cloud diagram of the Group C pier model (Figure 11), the Group C pier model in the displacement loading process stress state close to the displacement was equal when the Specimen C3 stress is the largest, Specimens A, C2 followed by the smallest C1, i.e., grouting sleeve connected to the precast assembled pier in the longitudinal reinforcement diameter was larger. In contrast, the displacement was the same when the pier's maximum stress was greater.

(2) Plastic Region Development. The plastic region cloud diagram from the Group C pier model (Figure 12) revealed that displacement was equal; Specimen C1 pier top and bottom had the most severe damage, the pier body damage was the lightest, whereas the Specimen C3 pier top and bottom of the damage was the lightest, the pier body damage was the most serious. The larger the diameter of the longitudinal reinforcement in the precast assembled pier connected using grouting sleeves, the damage at the top of the pier and the lower part of the pier in the area above the grouting sleeve was decreased, and the concrete damage in the body of the pier was aggravated.

5. Discussion

The prefabricated assembled bridge has a good application prospect because its construction process and assembling technology have gradually matured; however, only low-intensity areas apply prefabricated assembled technology because the prefabricated assembled bridge seismic theory is not yet perfect. Traditional cast-in-place bridge construction is completed as a whole; there is no relative displacement between piers, abutments, and cover beams under seismic action, and its seismic performance is only affected by a few factors, such as concrete strength, reinforcement rate, and axial compression ratio. The response of prefabricated assembled bridges connected using grouting sleeves under seismic action is more complicated, and factors such as the strength of grouting material, length of grouting sleeves, and diameter of reinforcement bars also have a greater effect on seismic performance. Scholars have studied the seismic performance of prefabricated precast assembled pier connected using grouting sleeves and clarified their damage modes and mechanisms. However, the effects of grout sleeve length, reinforcement diameter, and other factors on their seismic performance remain unclear. Therefore, based on the control variable method to establish different parameters of the prefabricated assembled piers model, we explored the response of prefabricated assembled piers under seismic action through the analysis of prefabricated assembled piers in the seismic action of hysteresis performance and damage mechanism, precise grouting sleeve length, reinforcing bar diameter grouting sleeve connected prefabricated assembled piers seismic performance of the influence of the grouting sleeve.

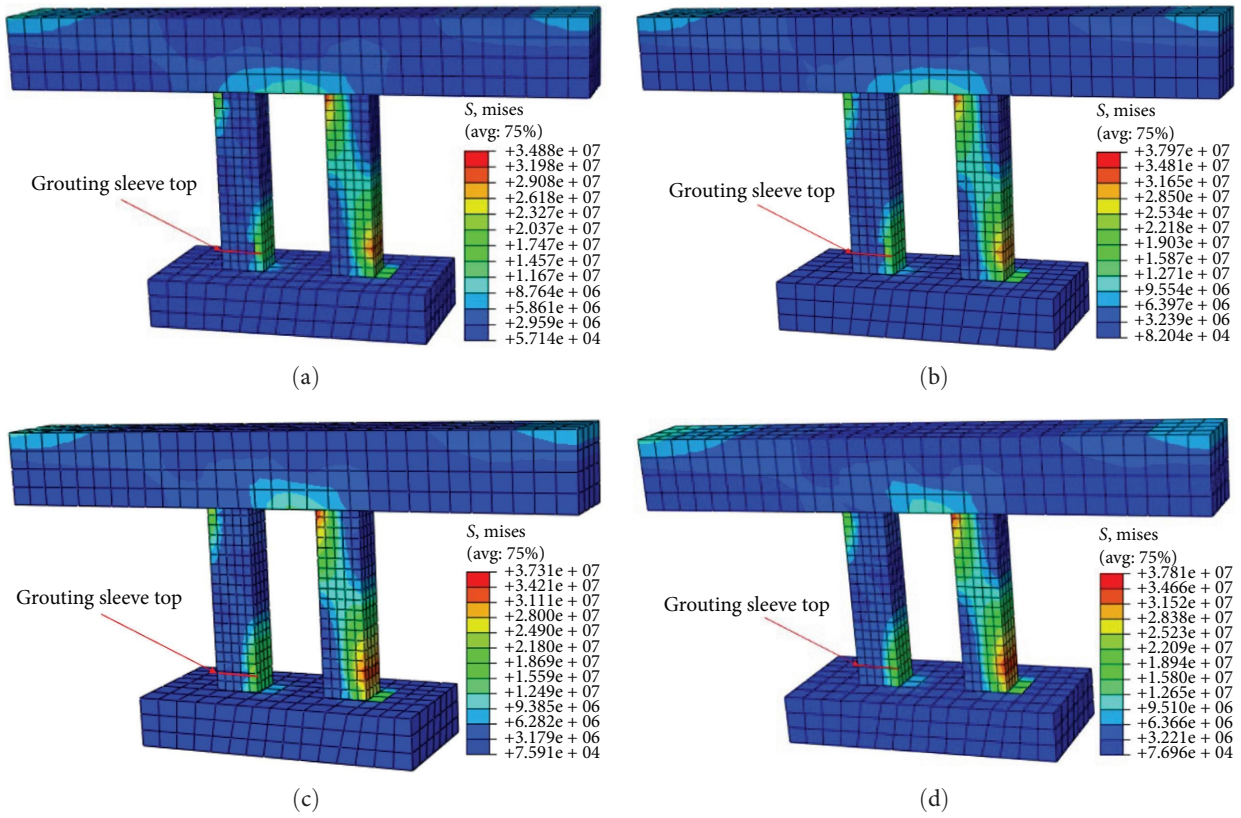

FIGURE 11: Stress cloud of Group B pier model displacement loaded to 40 mm: (a) test piece C1; (b) test piece C2; (c) test piece A; (d) test piece C3.

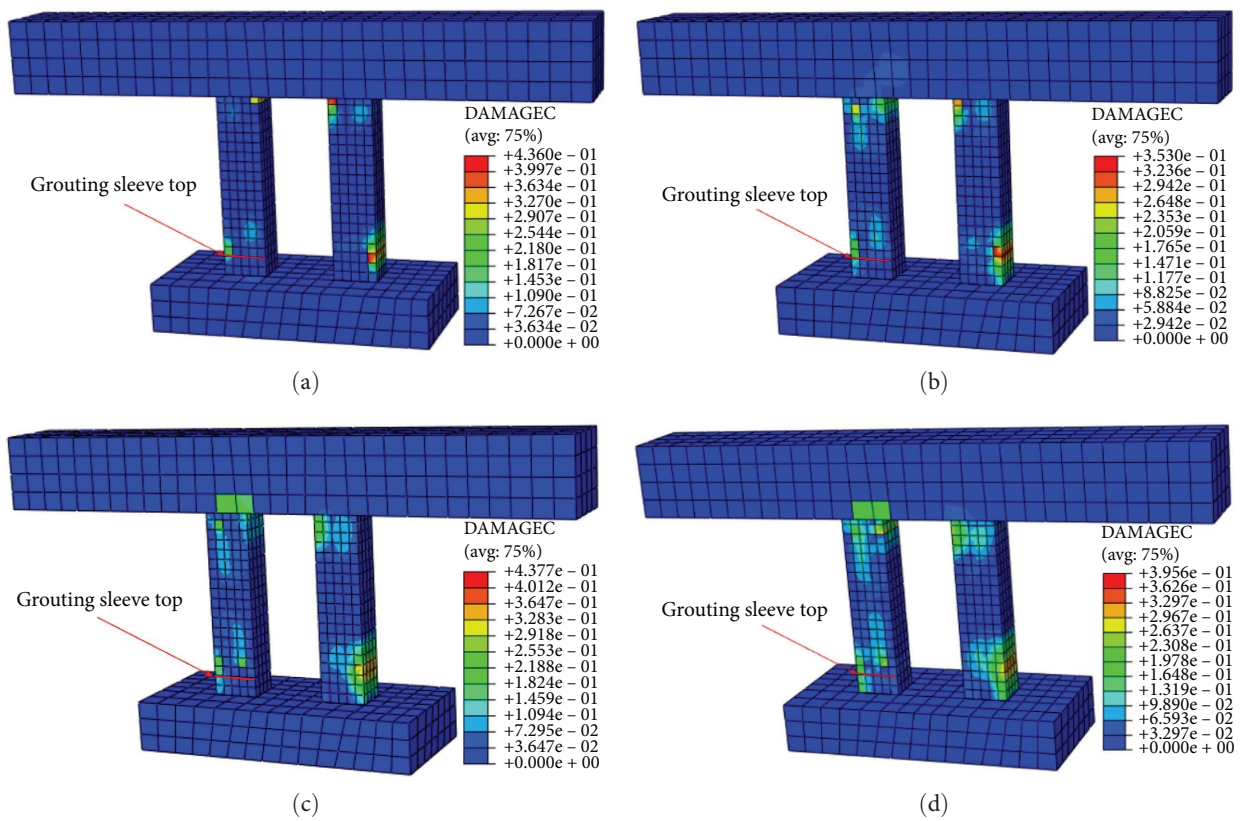

FIGURE 12: Plastic region cloud of Group B pier model displacement loaded to 40 mm: (a) test piece C1; (b) test piece C2; (c) test piece A; (d) test piece C3.

The reliability of the numerical simulation method used in this study was verified by comparing with the existing tests, relying on the actual project to establish a solid model of prefabricated assembled piers connected using refined grouting sleeves, applying low weekly reciprocating load to the model to simulate the seismic action, analyzing the response of prefabricated assembled piers under seismic action, and determining the effects of changing the diameter of reinforcement bars or the length of grouting sleeves on hysteresis performance and damage mechanisms of prefabricated assembled piers, so as to provide a reference and theoretical basis for the optimization of the design of bridges. However, the results of this study were not perfect because the proposed static method was not as accurate as the shaking table tests. Because the damage mode simulation of prefabricated piers by the proposed static method was not as accurate as the shaking table test, the effects of grouting sleeve length and reinforcement diameter on the seismic performance of prefabricated piers obtained in this study were not perfect, especially in terms of the damage mode of prefabricated piers under seismic action.

6. Conclusions

Through the finite element software ABAQUS to establish a refined solid model of the precast assembled pier, we applied low weekly reciprocating load to simulate the seismic action of the bridge piers, compared the reliability of the numerical simulation method with the existing test to verify the reliability of the numerical simulation method, analyzed the seismic performance of assembled piers in terms of hysteresis characteristics and damage mechanism, and studied the influence of the length of the sleeve and the diameter of the reinforcement bar on the seismic performance of assembled piers, and obtained the following conclusions:

(1) The maximum error between the numerical simulation results and the values of strength and deformation characteristics obtained from the test results was 5.7%; the stress concentration area of the precast assembled pier obtained from the numerical simulation in this paper is completely consistent with the test results, indicating that the numerical simulation method in this paper is reliable and feasible.

(2) Increasing the sleeve length can improve the yield load, yield displacement, peak load, and energy dissipation capacity of the assembled pier, but the peak displacement and ductility coefficient will be reduced, and the vulnerable parts of the assembled pier with the change of the location of the top of the sleeve changes; sleeve length were increased from 0.6 to 1.2 m, the peak load and cumulative dissipated energy by 10.9% and 11.4%, respectively. The change in the grouting sleeve length does not cause a significant difference in the residual displacement, but the pier ductility coefficient will decrease. Attention should be paid to the appropriate strengthening of the concrete strength of the top area of the sleeve to improve structural safety to improve the seismic performance of the bridge can be appropriate to increase the length of the sleeve.

(3) Increasing the diameter of reinforcement can improve the yield load, peak load, yield displacement, peak displacement, and energy dissipation capacity of the assembled pier. However, the residual displacement of the pier will increase, and the coefficient of ductility will decrease significantly. When the diameter of reinforcement was increased from 20 to 30, 40, and 50 mm, the peak load of the assembled pier increased by 26.9%, 57.0%, and 89.3%, respectively, and the dissipated energy increased by 59.1%, 131.6%, and 218.9%. However, their residual displacements increased by 51.8%, 99.8%, and 137.2%, respectively. When designing bridges to improve their load-carrying capacity and energy dissipation capacity by increasing the diameter of reinforcement, the problem of resetting the pier because of its excessive residual displacement should be prevented.

(4) Increasing the length of the grouting sleeve or increasing the diameter of longitudinal reinforcement will increase the pier stiffness, so that the top of the bridge pier to reach the same displacement of the load is larger. The damage is less severe, and the stress distribution is more uniform.

Data Availability

The data used in this work are available from the corresponding author by request.

Conflicts of Interest

The authors declare that they have no known competing financial interests or personal relationships that could have appeared to influence the work reported in this paper.

Acknowledgments

This research was supported by the National Science Foundation of China (51868041, 51668036), Basic Research Innovation Group Project of Gansu Province (21JR7RA347), Science and Technology Project of Gansu Province (21YF5GA050), Industrial Support Plan of Education Department of Gansu Province (2021CYZC-28), National Science Foundation of Gansu Province (22JR5RA338), and Key Research Program of Ningxia (2022BEG02056).

References

[1] F. Q. Chen, W. Tian, and L. S. Qin, "Research on hoisting equipment of pre-fabricated abutment and pier in Hong Kong-Zhuhai-Macao bridge," *Applied Mechanics and Materials*, vol. 256–259, pp. 1609–1613, 2012.

[2] E. Henin and G. Morcous, "Non-proprietary bar splice sleeve for precast concrete construction," *Engineering Structures*, vol. 83, pp. 154–162, 2015.

[3] M. J. Ameli, D. N. Brown, J. E. Parks, and C. P. Pantelides, "Seismic column-to-footing connections using grouted splice sleeves," *ACI Structural Journal*, vol. 113, no. 5, pp. 1021–1030, 2016.

[4] D. Guan, C. Jiang, Z. Guo, and H. Ge, "Development and seismic behavior of precast concrete beam-to-column connections," *Journal of Earthquake Engineering*, vol. 22, no. 2, pp. 234–256, 2018.

[5] Q. Yan, T. Chen, and Z. Xie, "Seismic experimental study on a precast concrete beam–column connection with grout sleeves," *Engineering Structures*, vol. 155, pp. 330–344, 2018.

[6] R. Chen, Y. Tan, B. Zhang, W. Shen, G. Liu, and Z. Wang, "Installation of integral prefabricated bridge abutment and pier with flexible water stop curtain," *Journal of Construction Engineering and Management*, vol. 144, no. 9, Article ID 04018087, 2018.

[7] I. De la Varga, R. P. Spragg, J. F. Muñoz, M. A. Helsel, and B. A. Graybeal, "Cracking, bond, and durability performance of internally cured cementitious grouts for prefabricated bridge element connections," *Sustainability*, vol. 10, no. 11, Article ID 3881, 2018.

[8] F. Seible, M. J. N. Priestley, and G. M. Calvi, *Seismic Design and Retrofit of Bridges*, John Wiley & Sons, 1996.

[9] Z.-Y. Bu, Y.-C. Ou, J.-W. Song, N.-S. Zhang, and G. C. Lee, "Cyclic loading test of unbonded and bonded posttensioned precast segmental bridge columns with circular section," *Journal of Bridge Engineering*, vol. 21, no. 2, Article ID 04015043, 2015.

[10] Z.-Y. Bu and Y.-C. Ou, "Erratum: simplified analytical pushover method for precast segmental concrete bridge columns (vol. 16, 805–822, 2013)," *Advances in Structural Engineering*, vol. 16, no. 6, 2013.

[11] C. Li, H. Hao, X. Zhang, and K. Bi, "Experimental study of precast segmental columns with unbonded tendons under cyclic loading," *Advances in Structural Engineering*, vol. 21, no. 3, pp. 319–334, 2018.

[12] C. Li, K. Bi, H. Hao, X. Zhang, and D. Van Tin, "Cyclic test and numerical study of precast segmental concrete columns with BFRP and TEED," *Bulletin of Earthquake Engineering*, vol. 17, pp. 3475–3494, 2019.

[13] C. Li, K. Bi, and H. Hao, "Seismic performances of precast segmental column under bidirectional earthquake motions: shake table test and numerical evaluation," *Engineering Structures*, vol. 187, pp. 314–328, 2019.

[14] Z. Lu, J. Huang, S. Dai, J. Liu, and M. Zhang, "Experimental study on a precast beam–column joint with double grouted splice sleeves," *Engineering Structures*, vol. 199, Article ID 109589, 2019.

[15] C. Ma, H. Jiang, and Z. Wang, "Experimental investigation of precast RC interior beam–column–slab joints with grouted spiral-confined lap connection," *Engineering Structures*, vol. 196, Article ID 109317, 2019.

[16] Y. Zhang, W. Fan, Y. Zhai, and W. Yuan, "Experimental and numerical investigations on seismic behavior of prefabricated bridge columns with UHPFRC bottom segments," *Journal of Bridge Engineering*, vol. 24, no. 8, Article ID 04019076, 2019.

[17] Y. Zhang, A. Tabandeh, Y. Ma, and P. Gardoni, "Seismic performance of precast segmental bridge columns repaired with CFRP wraps," *Composite Structures*, vol. 243, Article ID 112218, 2020.

[18] H. Liu, X. Wang, G. Tan, X. He, and G. Luo, "System reliability evaluation of prefabricated RC hollow slab bridges considering hinge joint damage based on modified AHP," *Applied Sciences*, vol. 9, no. 22, Article ID 4841, 2019.

[19] Z. Cheng and S. Sritharan, "Outdoor test of a prefabricated column–pile cap–pile system under combined vertical and lateral loads," *Journal of Bridge Engineering*, vol. 25, no. 8, Article ID 04020052, 2020.

[20] J. Jia, K. Zhang, M. S. Saiidi et al., "Seismic evaluation of precast bridge columns with built-in elastomeric pads," *Soil Dynamics and Earthquake Engineering*, vol. 128, Article ID 105868, 2020.

[21] Z. Wang, J. Wang, Y. Tang, Y. Gao, and J. Zhang, "Lateral behavior of precast segmental UHPC bridge columns based on the equivalent plastic-hinge model," *Journal of Bridge Engineering*, vol. 24, no. 3, Article ID 04018124, 2019.

[22] Z. Wang, J. Wang, G. Zhao, and J. Zhang, "Modeling seismic behavior of precast segmental UHPC bridge columns in a simplified method," *Bulletin of Earthquake Engineering*, vol. 18, pp. 3317–3349, 2020.

[23] B.-F. Wang, Q. Han, Z.-L. Jia, and X.-L. Du, "Seismic response analysis of the precast double-deck rocking frame bridge pier system," *Soil Dynamics and Earthquake Engineering*, vol. 146, Article ID 106745, 2021.

[24] Y. Han, J. Dong, and L. Wang, "Experimental study on the seismic performance of socket bridge piers," *Advances in Civil Engineering*, vol. 2020, Article ID 8895196, 10 pages, 2020.

[25] Z. B. Haber, K. R. Mackie, and H. M. Al-Jelawy, "Testing and analysis of precast columns with grouted sleeve connections and shifted plastic hinging," *Journal of Bridge Engineering*, vol. 22, no. 10, Article ID 04017078, 2017.

[26] Y. Liu, X. Li, X. Zheng, and Z. Song, "Experimental study on seismic response of precast bridge piers with double-grouted sleeve connections," *Engineering Structures*, vol. 221, Article ID 111023, 2020.

[27] Y. L. Woong, S. Jihye, K. Seungjun, K. Jong, and W. Deokhee, "Cyclic lateral performance evaluation of precast double-skinned composite tubular columns," *International Journal of Steel Structures*, vol. 18, pp. 97–113, 2018.

[28] J. Jia, K. Zhang, S. Wu, Y. Guo, X. Du, and X. Wang, "Seismic performance of self-centering precast segmental bridge columns under different lateral loading directions," *Engineering Structures*, vol. 221, Article ID 111037, 2020.

[29] H. Dawood, M. ElGawady, and J. Hewes, "Behavior of segmental precast posttensioned bridge piers under lateral loads," *Journal of Bridge Engineering*, vol. 17, no. 5, pp. 735–746, 2012.

[30] F. Yuan, Y.-F. Wu, and C.-Q. Li, "Modelling plastic hinge of FRP-confined RC columns," *Engineering Structures*, vol. 131, pp. 651–668, 2017.

[31] J. P. Ge, X. F. Yan, and Z. Q. Wang, "Seismic performance of precast assembled piers connected by grouting sleeves and prestressed tendons," *Transportation Engineering Journal*, vol. 18, no. 2, pp. 42–52, 2018.